Experimental study of hot-rolled rectangular hollow sections

A. Liew[1], N. Boissonnade[2], L. Gardner[3], J. Nseir[4]

Abstract

Hot-rolled structural steel hollow sections typically display largely homogeneous material properties around the cross-section with low residual stresses, due to the uniform cooling pattern associated with the production of uniform sections of constant thickness. This leads to a stress-strain response with a clearly defined yield stress and an extended yield plateau. To examine the behaviour of such members, tests were carried out on hot-rolled structural steel rectangular hollow sections, including material tests and experiments on stub columns, simply supported beams, continuous beams and propped cantilevers. Two wall thicknesses were considered which gave compact cross-sections according to AISC 360-10 (2010), yet most test specimens did not reach their designated plastic design values. Failure by local buckling occurred during the extended material yield plateau, and did not allow for the benefits from strain hardening that are implicitly assumed for the attainment of the plastic moment capacity. Tests on elements in indeterminate configurations showed that system peak loads can occur when some cross-sections are unloading, having already passed their peak moments. Plotting rotation-curvature curves at hinge locations showed that the hinge rotations from an idealised plastic collapse geometry, are proportional to curvatures only during the elastic loading phase. This proportional relationship deteriorated once cross-section yielding had occurred, as curvatures measured by post-yield strain gauges rapidly accelerated when compared to the rotations measured from inclinometers.

---

[1] Researcher, Imperial College London, <andrewtliew@gmail.com>
[2] Professor, University of Applied Sciences of Western Switzerland, <Nicolas.Boissonnade@hefr.ch>
[3] Professor, Imperial College London, <leroy.gardner@imperial.ac.uk>
[4] Researcher, University of Applied Sciences of Western Switzerland, <joanna.nseir@gmail.com>

1 Introduction

Hot-rolled structural steel hollow sections typically exhibit uniform material properties and low residual stresses due to their uniform cooling. This leads to a material stress-strain response that displays a sharply defined yield stress and an extended yield plateau, with material properties similar around the entire cross-section. This differs from the behaviour of hot-rolled I-sections which can show variations in material properties due to the different cooling rates for the flanges, webs and web-flange junctions (Alpsten (1968), Byfield and Nethercot (1997)). To examine the behaviour of such members, a set of hot-rolled rectangular hollow sections were tested in the Civil Engineering laboratory at the University of Applied Sciences of Western Switzerland in Fribourg, as part of a collaboration with Imperial College London. Similar tests to those investigated in this study were performed by Gardner et al. (2010) on hot-rolled and cold-formed rectangular hollow sections. Specimens were cut from eight members for tests on tensile coupons, stub columns, simply supported beams in four-point bending, continuous beams and propped cantilevers. For the indeterminate configurations, all beams had the same spans between supports, and were loaded at two locations by concentrated loads. The tests were primarily aimed at providing data on ultimate load carrying capacities, as well as rotations and curvatures in the inelastic range at plastic hinge locations.

In the current European design code, EN 1993-1-1 (2005), and the American code AISC 360-10 (2010), structural steel cross-sections are limited in resistance to the yield load $N_y=Af_y$ in compression and the plastic moment $M_{pl}=W_{pl}f_y$ in bending, where A is the cross-section area, W_{pl} is the plastic section modulus and f_y is the material yield stress. The plastic moment resistance, which is based on a stress distribution entirely at the yield stress, cannot be obtained if material stresses are limited to f_y, as stresses below the yield stress will exist near the neutral axis, though it is often assumed in design that strain hardening will enable moment resistances to achieve the plastic moment. Various methods exist for allowing cross-section capacities greater than N_y and M_{pl}. Kemp et al. (2002) described a bi-linear moment-curvature model based on bending tests of hot-rolled I-sections, and Byfield and Nethercot (1998) put forward two models for incorporating strain hardening into the design of I-section beams, by using the material stress at a strain of 1.5 %. The Continuous Strength Method as detailed in Gardner et al. (2011), describes an approach that allows for cross-section capacities greater than N_y and M_{pl} by utilising a strain based design approach with a bi-linear material model, defined with a strain hardening modulus E_{sh} (taken for structural steel as 0.01 times the Young's modulus E).

2 Material testing

Tensile coupon tests were performed on material extracted from the flat faces of the members away from the weld location. A total of 32 coupons were tested. The identification convention consists first of the member number, then C for coupon test, followed by the thickness, and finally by the face number; for example coupon 2C41 is from member number 2, of 4 mm thickness and taken from face 1. The coupons were 300 mm long with nominal cross-section dimensions of 5 mm×10 mm or 4 mm×10 mm, and the material had a nominal yield stress of 355 N/mm^2. After cutting the coupons and edge cleaning, the cross-section dimensions b (width) and t (thickness) were recorded by a micrometer at three locations along the middle of the coupons. Once a coupon was gripped in the testing rig (Fig. 1), a 20 mm clip gauge was attached, and a constant rate of strain (0.045 %/s) was applied for 10-15 minutes until fracture. Of the 32 coupon tests only 1C44 and 4C52 had measurement issues related to the ultimate and fracture strains, and coupon 4C54 was not tested due to cutting complications.

Figure 1: Tensile coupon specimen and attached clip gauge

Two of the stress-strain curves are plotted in Fig. 2, which show that after the initial elastic region a yield plateau is observed, before strain hardening initiates up until the ultimate stress. The recorded yield stress f_y was taken as the average of the yield plateau between the strains of 0.5 % and 3 %, while the Young's modulus E was taken as the gradient between 20 % and 80 % of f_y. All coupon data are summarised in Table 1, in which f_u is the ultimate tensile stress, ε_u is the strain at the ultimate tensile stress and ε_f is the fracture strain over a 20 mm gauge length.
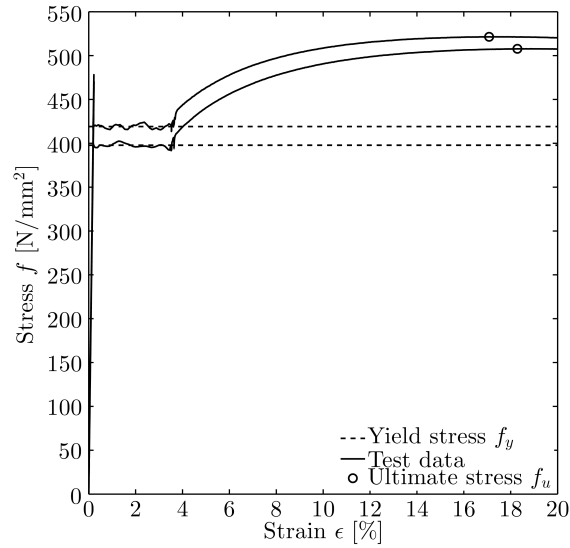
Figure 2: Stress-strain curves for 5 mm coupon 2C54 (lower curve) and 4 mm coupon 3C41 (upper curve)

3 Stub columns

Stub columns of length L=370 mm, provided specimens that were three times longer than the cross-section depth. The nominal depth and width of the cross-sections were D=120 mm and B=80 mm, with two wall thicknesses, t=4 mm and t=5 mm. The identifiers are such that 2ST5 represents the stub column from member 2 of 5 mm wall thickness. Cross-section dimensions were recorded by micrometer at both ends of the stub columns and repeat measurements were taken, with the averaged values summarised in Table 2. The internal root radii were found to be approximately equal to the wall thickness t. The stub columns were weighed before testing and the mass, cross-section dimensions and assumed density of 7850 kg/m³ were used to calculate the cross-section area A. High strength steel end-plates of size 250 mm×250 mm×15 mm were used at each stub column end. An array of four 50 mm induction displacement transducers were positioned at the corners of the bottom end-plate to measure the overall end-shortening. Four strain gauges were attached to the column mid-faces to get the true local strains. These strain gauges were HBM 120 Ω resistance and 10 mm in length. The testing machine was a 3000 kN capacity Walter+Bai hydraulic rig. Fig. 3 shows a stub column, with the end-plates, strain gauges and displacement transducers. The specimens were loaded under displacement control beyond their peak loads, with the rate of displacement kept constant at 0.025 mm/s until the peak load, and then the rate increased soon after. The locally deformed shapes consisted of inward and outward buckles on alternate faces. For five of the stub columns these buckles formed near the column bases (1ST4, 2ST4, 3ST4, 2ST5 and 3ST5), for two specimens the local buckling occurred at mid-height (4ST4 and 4ST5) and for 1ST5 they formed near the top. Photos of two 4 mm thickness stub columns after testing are shown in Fig. 4. Since there were differences between the end-shortening measurements from the displacement transducers and those calculated from the strain gauges, a correction was required that combined both sets of measurements. To calculate the correct end-shortening δ_c, the method described by the Centre for Advanced Structural Engineering (1990) was used, which assumes any additional set-up effects are elastic and proportional to the applied stress.

4

Table 1: Tensile coupon measured geometry and calculated material properties (E_{avg}, $f_{y,avg}$ and $f_{u,avg}$ are the averaged Young's moduli, yield stresses and ultimate stresses respectively)

ID	b	t	E	f_y	f_u	ε_u	ε_f	E_{avg}	$f_{y,avg}$	$f_{u,avg}$
	mm	mm	N/mm^2	N/mm^2	N/mm^2	%	%	N/mm^2	N/mm^2	N/mm^2
1C41	9.99	3.89	203100	441	537	16.7	26.6	203600	436	534
1C42	10.10	3.92	201100	419	522	17.0	27.1			
1C43	10.05	3.83	196500	440	535	16.2	23.5			
1C44	10.06	3.86	213600	444	541	-	-			
2C41	10.08	4.02	194200	420	519	17.3	27.3	198200	423	524
2C42	10.15	3.90	192500	415	518	17.4	26.9			
2C43	10.08	3.80	202400	429	529	16.8	26.7			
2C44	10.09	3.83	203700	428	532	17.0	26.7			
3C41	10.06	3.88	214600	419	521	17.1	27.5	207700	419	521
3C42	10.04	4.05	205700	406	505	17.6	26.5			
3C43	10.02	3.86	205000	424	530	17.5	26.7			
3C44	10.05	3.81	205500	428	526	17.7	27.8			
4C41	10.12	3.94	217400	413	512	17.5	26.6	208300	423	523
4C42	10.07	3.85	199000	418	522	17.6	26.0			
4C43	10.04	3.84	208700	429	527	17.4	26.9			
4C44	10.01	3.87	208300	430	533	17.9	27.7			
1C51	10.08	4.67	199000	394	506	18.5	28.5	197300	396	503
1C52	10.20	4.80	199200	391	499	18.0	28.3			
1C53	10.18	4.75	194800	399	504	18.8	27.8			
1C54	10.15	4.77	196000	398	503	18.5	29.4			
2C51	10.19	4.84	204000	400	503	18.7	28.6	207700	401	506
2C52	10.11	4.66	200600	404	509	18.3	28.7			
2C53	10.17	4.74	218700	404	505	18.8	27.9			
2C54	10.10	4.72	207500	398	508	18.3	27.6			
3C51	10.03	4.63	204900	398	513	18.8	28.3	203000	400	509
3C52	10.04	4.83	203800	398	507	18.4	29.1			
3C53	10.07	4.68	201500	404	509	19.3	27.6			
3C54	10.09	4.75	201800	400	508	18.7	30.2			
4C51	10.01	4.68	206000	398	508	19.0	29.3	206100	395	506
4C52	10.20	4.89	214700	391	499	-	-			
4C53	10.06	4.73	197400	397	510	18.8	29.1			
4C54	-	-	-	-	-	-	-			

In Fig. 5 the stub column axial load N is normalised by the yield load N_y (calculated as the product of the cross-section area A and the tensile coupon yield stress f_y), the end-shortening δ_c is divided by the initial length L, and the measured strains ε are divided by the yield strain ε_y (from measured f_y and E). For the 4 mm stub columns, the peak loads are reached soon after yielding, post-peak unloading occurs suddenly and the axial loads drop.

Table 2: Measured geometric properties and normalised ultimate loads N_u/N_y from the stub column tests

ID	D	B	t	L	A	N_u/N_y
	mm	mm	mm	mm	mm^2	
1ST4	119.71	80.13	3.87	368	1478	1.052
2ST4	119.69	80.07	3.88	369	1474	1.068
3ST4	119.71	80.24	3.90	366	1495	1.067
4ST4	119.61	80.12	3.91	369	1479	1.060
1ST5	119.65	80.23	4.78	368	1784	1.042
2ST5	119.76	80.23	4.76	366	1787	1.012
3ST5	119.71	80.30	4.76	368	1787	1.043
4ST5	119.75	80.26	4.75	368	1790	1.048
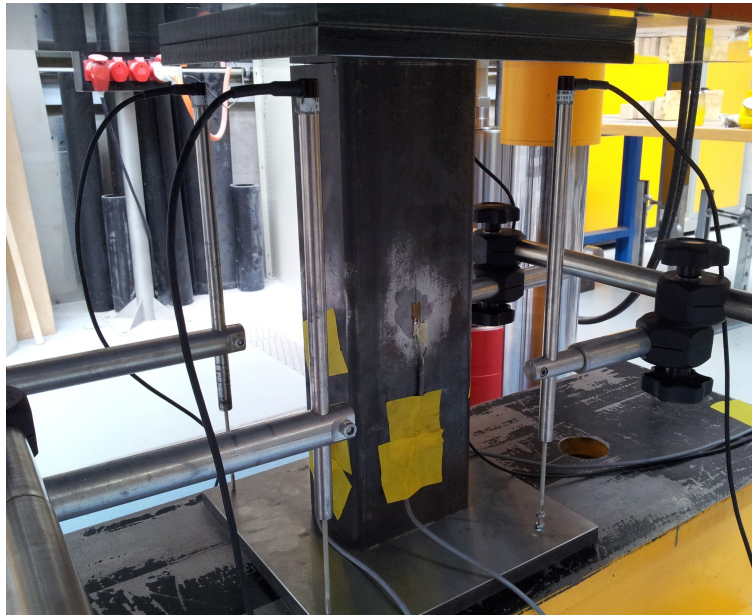
Figure 3: Stub column specimen with strain gauges and displacement transducers

There is a distinction between the behaviour of the 5 mm and 4 mm plate thickness columns, as the normalised peak loads are similar, but the 5 mm thickness columns take significantly longer to unload. The average normalised peak load N_u/N_y for the four 4 mm stub columns is 1.062 and the average peak strain is 0.256 %. The average normalised peak load for the 5 mm stub columns (excluding 2ST5) is 1.044 and the average peak strain is also 0.256 %.
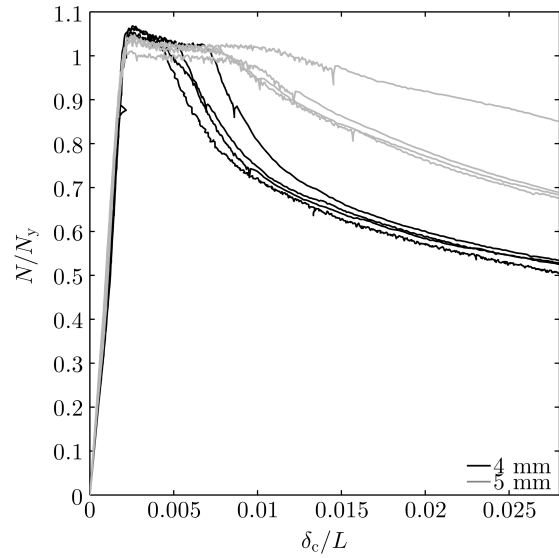
Figure 4: 4 mm post-test deformed stub columns 3ST4 and 4ST4

Figure 5: Normalised load vs end-shortening plots for the tested stub columns

4 Simply supported beams

Two simply supported beams of total length L_T=2500 mm were tested under four-point bending. The identifiers for these two members are SS5.4P and SS4.4P for the nominal t=5 mm and t=4 mm thicknesses respectively. The experimental set-up is shown in Fig. 6, the post-test deformed state of beam SS5.4P is given in Fig. 7, and the cross-section geometries are summarised in Table 3. The nominal cross-section depth and width for both members were D=120 mm and B=80 mm. The final 100 mm of both beam ends overhung the support center-lines, giving spans of L=2300 mm.
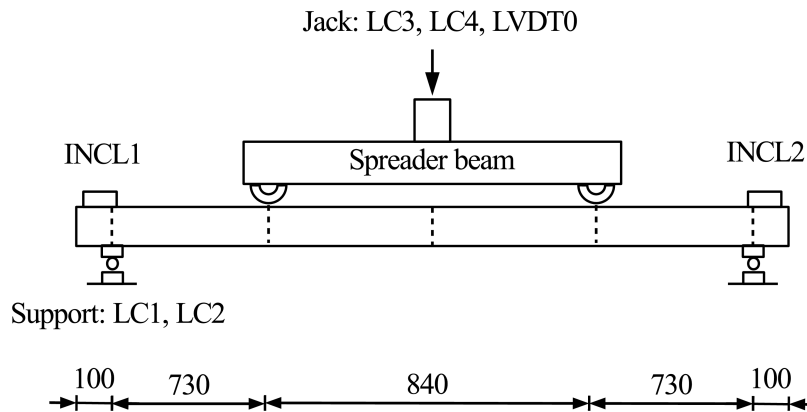
Figure 6: Test set-up for the four-point bending of SS5.4P and SS4.4P (dimensions in mm)

Figure 7: Post-test deformed shape of beam SS5.4P

The two beams were loaded under displacement control via a loading bridge that consisted of the following features: An I-section beam was connected to a strong floor by two high-strength 32 mm diameter bars, which were threaded through two thick plates mounted on the top flange of the floor beam. Connected into the top flange of the floor beam were two 250 kN hydraulic jacks, each supported by four threaded bars. Load cells LC3 and LC4 (Fig. 6), which were located underneath the jacks, measured the jack forces, and a single displacement transducer LVDT0 fed the bridge vertical displacements to the hydraulic control panel. A rectangular hollow section cross-beam was used to link the two jacks, and was supported by threaded bars that passed through the center of the jacks. The cross-beam was then bolted into a double webbed I-section spreader beam, which had half-round loading points screwed into the underside of the beam. The jacks were each pre-loaded with 5.0 kN of force by zeroing the load cells and then tightening the end nuts during live measurement readings. The weights of the cross-beam and the spreader beam were recorded, and then added to the pre-load force. Roller supports were arranged at each beam end, with the right support layered with a film of grease between the underside of the beam and the supporting plate, and two load cells LC1 and LC2 were placed underneath the left support. The plates supporting the beams were 80 mm wide and 30 mm thick, rested upon 30 mm diameter rollers. The plate and roller pairs were positioned between angles that were stiffened by welded plates, and with gaps left to allow for the activation of the load cells. The support angles were bolted into I-section columns that were anchored into the strong floor by threaded bars.

Instrument readings were monitored at a frequency of 2 Hz through HBM CatmanEasy software and using HBM Spider8 data acquisition hardware. Several low load elastic cycles were initially performed to achieve load symmetry between the jacks and for verticality of the loading bridge. Loads up to the peak load gave deflected beam shapes that were approximately symmetric, but for post-peak unloading the beam deflections favoured the right and left loading points for the SS5.4P and SS4.4P beams respectively. The maximum deflections at the peak loads were approximately 25 mm.

Table 3: Measured geometry and normalised ultimate moments M_u/M_{pl} for the simply supported four-point bending tests

ID	D	B	t	M_u/M_{pl}
	mm	mm	mm	
SS4.4P	119.58	80.12	3.91	0.9439
SS5.4P	119.64	80.21	4.71	0.9252

Inclinometers INCL1 and INCL2 were fixed at both beam ends to record the end rotations θ. In the moment-rotation curves of Fig. 8, the rotations are normalised by the yield rotations θ_y and paired with the moments M under the point loads, divided by the plastic moments as calculated from the measured cross-section properties. The yield rotation θ_y is the rotation at the beam ends when the middle segment cross-sections first reach the elastic moment $M_{el}=W_{el}f_y$, where W_{el} is the elastic section modulus. For both beams, local buckling inhibited the tested hot-rolled cross-sections from strain hardening and reaching the plastic moments.
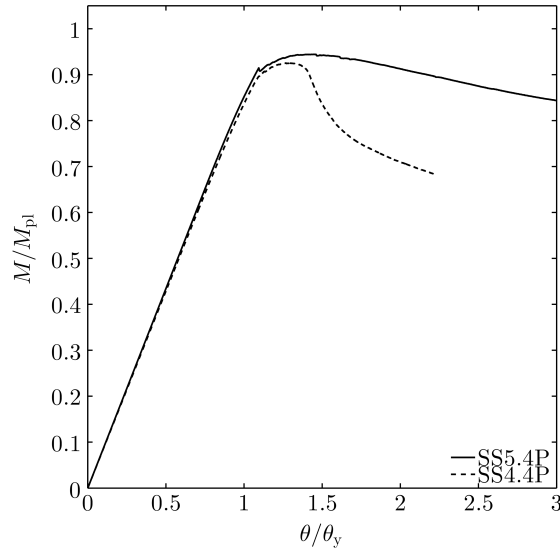
Figure 8: Normalised moment-rotation response from simply supported four-point bending tests

5 Continuous beams

Four continuous beams with equal spans of L=2300 mm (i.e. with reference to Fig. 9, $a+b$=2300) and total lengths L_T=5000 mm were tested. Two of the beams were loaded centrally, with the concentrated loading points at the middle of each span, and two beams were loaded off-center. The test set-up in Fig. 9 was identical for both loading configurations except for the movement of the loading bridges away from the mid-spans and to the outer third points for the outer loading arrangement. The identifiers for the 4 mm and 5 mm wall thickness continuous beams are CO4.C and CO5.C for the centrally loaded beams, and CO4.O and CO5.O for the 4 mm and 5 mm outer loaded beams. Load cells were located in pairs at each of the two loading bridges and at the middle supports. Load cells LC5 and LC6 measured the forces in the left-side jacks, LC3 and LC4 were situated at the right-side jacks, and LC1 and LC2 measured the support reaction at the

central supports. The spans were loaded under displacement control, based on the displacements from an LVDT on the right loading beam. The hydraulic system was a single oil circuit rig, chosen to encourage even displacements across both loading bridges. However in the final displaced shape of the centrally loaded beams, both spans did not displace at the same rate, particularly after the peak system loads (Fig. 10). The left and right spans of the outer loaded beams had very similar vertical deflections throughout testing, showing no bias to either side. The cross-section geometry and the test collapse load P_u, normalised by the calculated plastic collapse load P_{pl}, are summarised in Table 4.
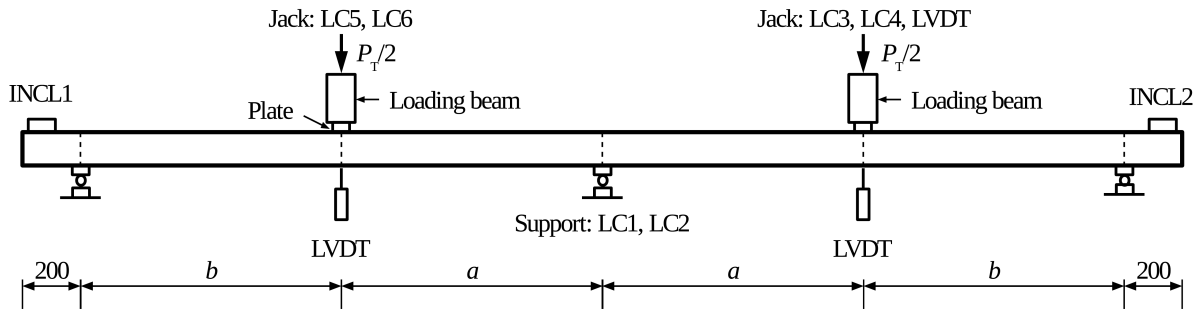
Figure 9: Continuous beam configuration (centrally loaded $a=b=1150$ and outer loaded $a=1533$, $b=767$ [mm])

Table 4: Measured cross-section geometry and normalised collapse loads
for the continuous beam tests

ID	D	B	t	P_u/P_{pl}
	mm	mm	mm	
CO4.C	119.61	80.12	4.05	0.896
CO5.C	119.45	80.12	4.76	0.952
CO4.O	119.64	80.24	3.90	0.941
CO5.O	119.72	80.27	4.79	0.920

Figure 10: Deformed shape of continuous beam CO5.C after testing

In Fig. 11 to Fig. 14, the moments M at the spans and the supports are normalised by the plastic moments calculated from the measured cross-section geometry and yield stress, and plotted against the rotations θ at the left support from inclinometer INCL1.
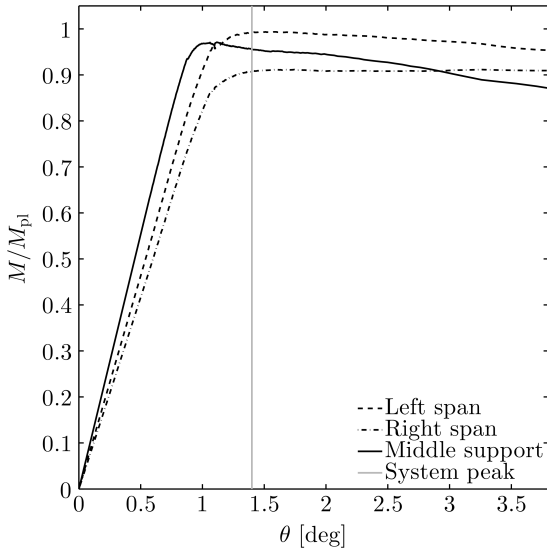
Figure 11: Moment-rotation curves for CO5.C
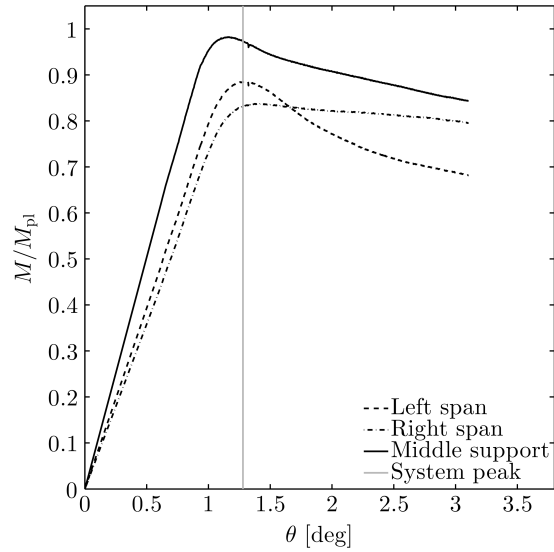
Figure 12: Moment-rotation curves for CO4.C
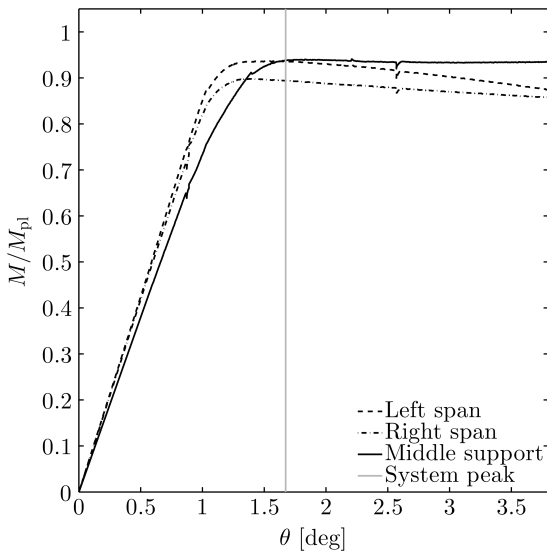
Figure 13: Moment-rotation curves for CO5.O
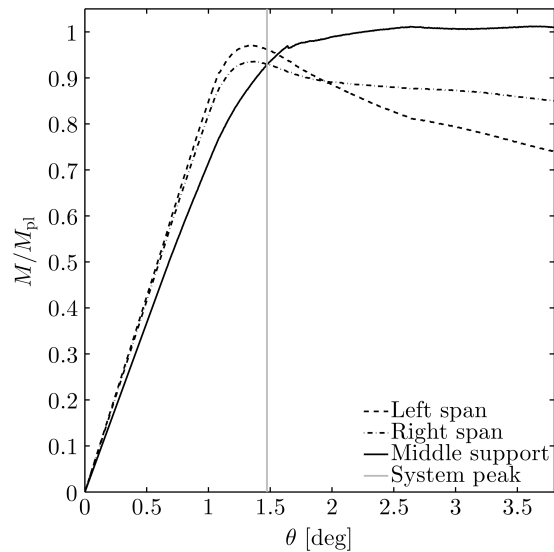
Figure 14: Moment-rotation curves for CO4.O

For the centrally loaded beams (shown in Fig. 11 and Fig. 12), the middle supports initially attract (in the elastic phase) higher moments relative to the span moments; after the peak system loads, the curves decline gradually for CO5.C and more sharply for CO4.C. The system peak

11

loads are beyond the peak moments of the middle supports. For both of the centrally loaded continuous beams there was a bias to the left spans, as they deflected the greatest and had the highest peak moments. For the outer loaded continuous beams the moment-rotation curves were close to overlapping, as seen in Fig. 13 for beam CO5.O and in Fig. 14 for beam CO4.O. For these beams the span moments at the loading points were initially higher than the middle support moments and peaked at approximately the same rotations. The support moments exceeded the span moments as the spans unloaded, and the system peak loads occurred before the central supports reached their peak moments.

In Fig. 15 and Fig. 16, the continuous beam total loads P_T are normalised by the traditional plastic collapse loads P_{pl}, and plotted against the maximum vertical deflections v_m, which are the larger of the left and right span deflections. The plastic collapse loads were calculated using the method of virtual work with idealised plastic hinges rotating at the plastic moment M_{pl}. As the plastic moments were not consistently attained in the continuous beam tests the plastic loads overestimate the attained test collapse loads, with the peak to plastic collapse load ratios P_u/P_{pl} between 0.90 and 0.95 (Table 4).
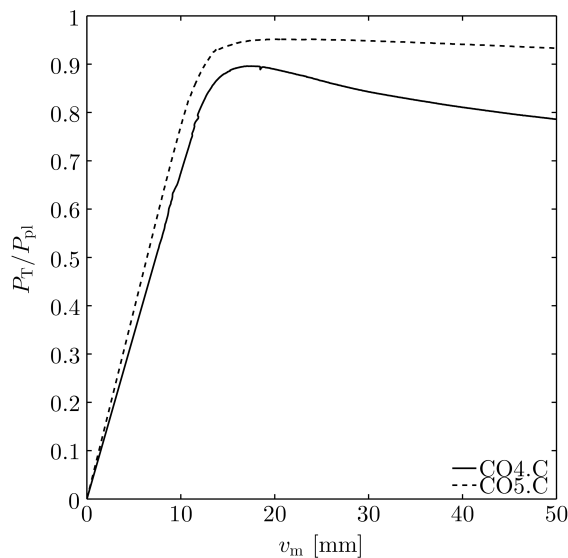
Figure 15: Normalised total load-maximum displacement curves for the centrally loaded continuous beams
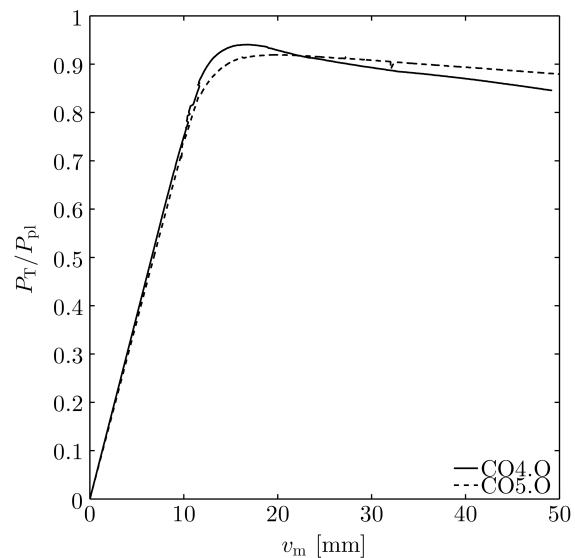
Figure 16: Normalised total load-maximum displacement curves for the outer loaded continuous beams

6 Propped cantilevers

Four propped cantilever beams were tested, PR4.C and PR5.C, of 4 mm and 5 mm thickness respectively and loaded at the middle of the total length L_T, close to the mid-span, and PR4.O and PR5.O tested with the concentrated loads located closer to the propped supports (Fig. 17). The beam spans were L=2300 mm with additional overhangs of 200 mm, and with the measured cross-section dimensions given in Table 5. At the left propped support, load cell LC1 was used to measure the support reactions, and inclinometer INCL1 was fastened to the beams to record the left end rotations.
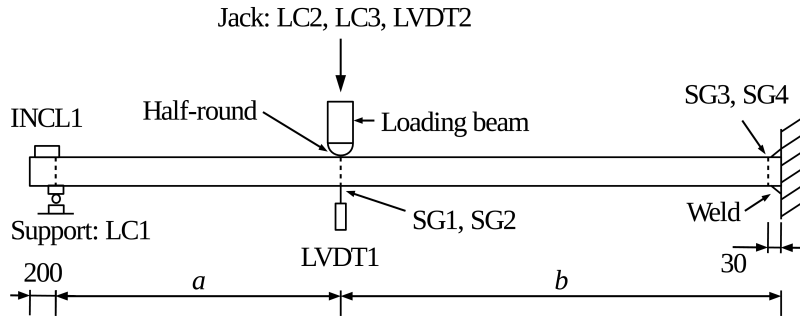
Figure 17: Propped cantilever tests (centrally loaded *a*=1050, *b*=1250 and outer loaded *a*=767, *b*=1533 [mm])

Table 5: Measured cross-section geometry and normalised collapse loads
for the propped cantilever tests

ID	D	B	t	P_u/P_{pl}
	mm	mm	mm	
PR4.C	119.67	80.19	3.87	0.859
PR5.C	119.69	80.14	4.76	0.895
PR4.O	119.68	80.12	3.88	0.888
PR5.O	119.72	80.19	4.74	0.856

The end-plate and its bolted connection into a supporting frame, used at the fixed ends of the propped cantilevers, is pictured in Fig. 18. Eight 8.8 M24 bolts were used, with passes of 4 mm full penetration weld to ensure rigidity at the fixed connection. Two pairs of TML YMFA-10 post-yield strain gauges (10 mm gauge length) were glued with epoxy resin at the expected hinge locations, strain gauges SG1 and SG2 located under the applied load and SG3 and SG4 at the fixed support. Strain gauges SG3 and SG4 were attached to the closest flat surfaces next to the welds, which gave a 30 mm distance between the end-plate face and the strain gauge centers.

Figure 18: Frame to beam fixed end connection

The selected 20 mm thick end-plates were found to be sufficiently thick for essentially fixed behaviour; such a thickness was found to be suitable for fixed conditions with rectangular hollow sections of larger dimensions from the experimental research of Wheeler et al. (1998).

Figure 19: Propped cantilever after testing
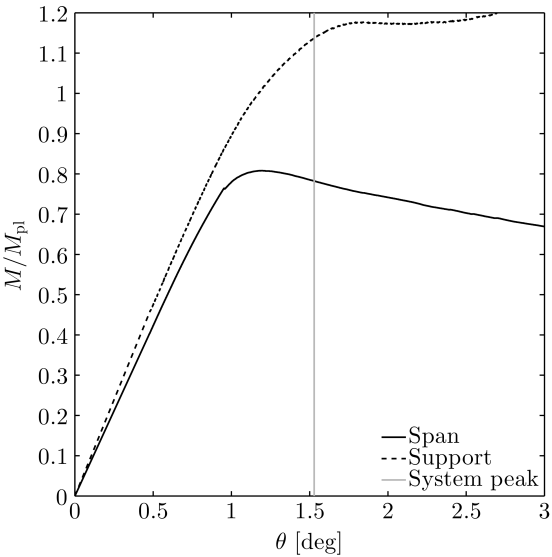
Figure 20: Normalised moment-rotation curves for the centrally loaded propped cantilever PR5.C
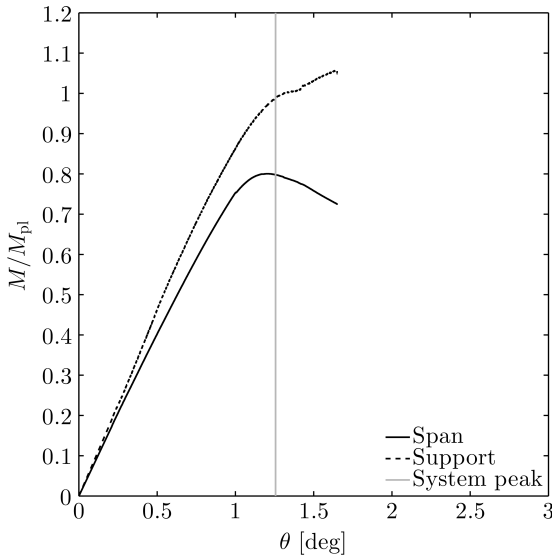
Figure 21: Normalised moment-rotation curves for the centrally loaded propped cantilever PR4.C

The moment-rotation curves using rotations θ from INCL1 are plotted in Fig. 20 and Fig. 21 for the centrally loaded propped cantilevers. The fixed support moments were higher than the span moments, and the curves separate at end rotations of around 1 degree. For the outer loaded propped cantilevers, plotted in Fig. 22 and Fig. 23, the initial span moments were greater than the fixed end moments up until just after the peak span moments, which occurred at rotations of $\theta \approx 1.2$ degrees. For both loading set-ups the span peak moments were less than the plastic moments as local buckling caused the cross-sections to fail prematurely. However, the support cross-sections, which had additional restraint from the welded end connection, were more resistant to local buckling and obtained moments greater than the plastic moments in the centrally loaded case.
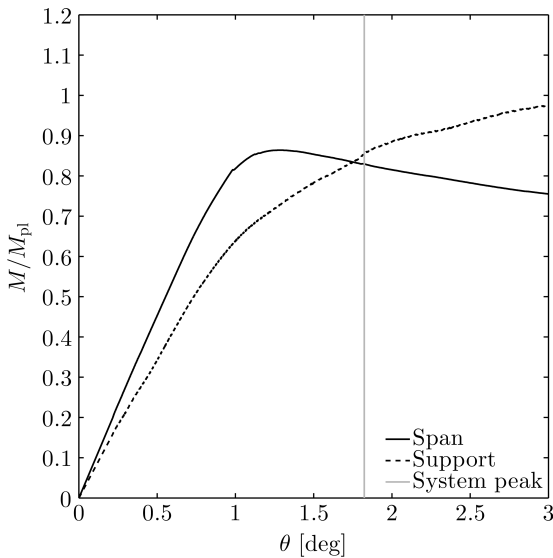
Figure 22: Normalised moment-rotation curves for the outer loaded propped cantilever PR5.O
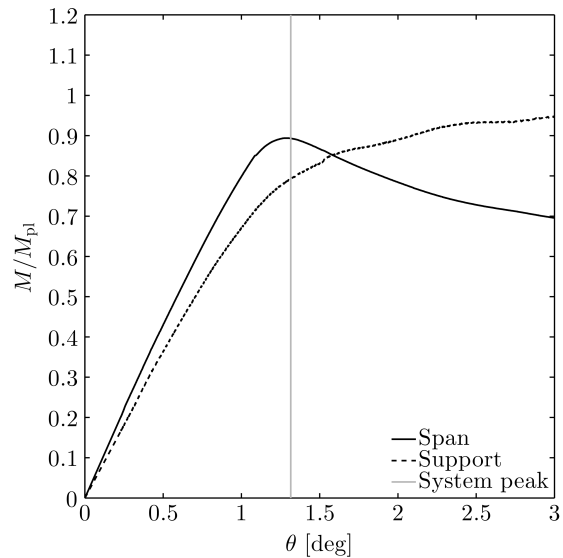
Figure 23: Normalised moment-rotation curves for the outer loaded propped cantilever PR4.O

The peak system loads were at rotations beyond the occurrence of the peak moments in the spans, and occurred while the support moments were still increasing. From the strain gauge measurements and a plane sections remain plane assumption, the curvatures at the cross-sections can be determined. These curvatures can be used to plot moment-curvature curves such as those in Fig. 24, or to plot the yield normalised hinge rotation-curvature curves of Fig. 25 and Fig. 26. For a representative yield rotation θ_y to normalise to in the rotation-curvature plots, the rotations to consider are the hinge rotations in a traditional plastic collapse analysis at first yield, and the yield curvature is defined as $\kappa_y = M_{el}/EI$ where EI is the flexural rigidity of the beam cross-sections. The important observation is that the yield normalised curvatures and rotations are not proportional in the inelastic range. In both Fig. 25 and Fig. 26, after the proportional relationship in the elastic region, both the spans and the fixed supports give curvatures that increase rapidly after first yielding.
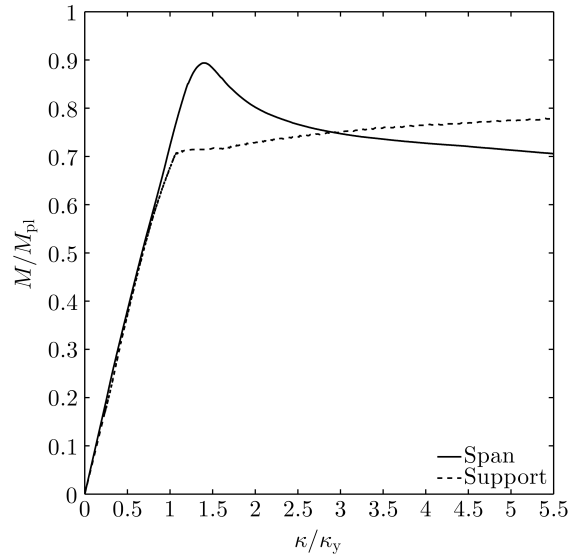
Figure 24: Normalised moment-curvature curves for the outer loaded propped cantilever PR4.O
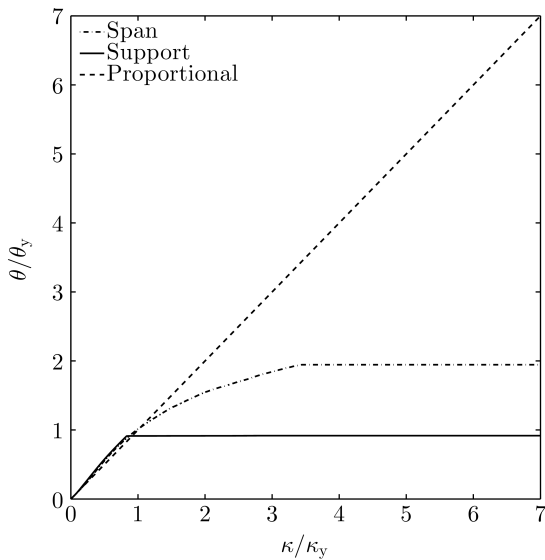
Figure 25: Normalised hinge rotation-curvature plots for the centrally loaded propped cantilever PR5.C
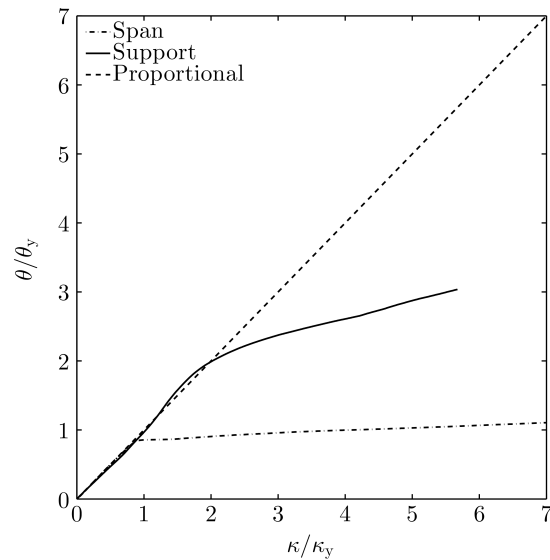
Figure 26: Normalised hinge rotation-curvature plots for the outer loaded propped cantilever PR4.O

The total applied loading P_T for the centrally loaded and outer loaded propped cantilevers are normalised respectively in Fig. 27 and Fig. 28 by the plastic collapse loads P_{pl}, and plotted against the maximum span deflections v_m. For the centrally loaded propped cantilevers, the peak load for PR5.C occurred at larger vertical deflections than PR4.C, and also obtained a greater collapse load of P_u/P_{pl}=0.895 compared to P_u/P_{pl}=0.859.
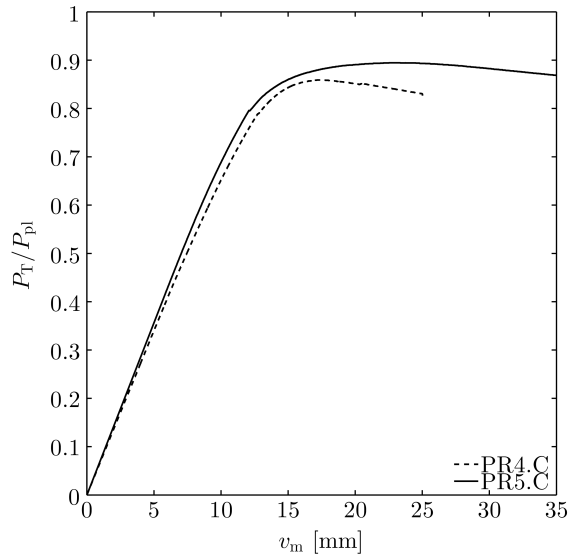
Figure 27: Normalised total load-maximum displacement curves for the centrally loaded propped cantilevers
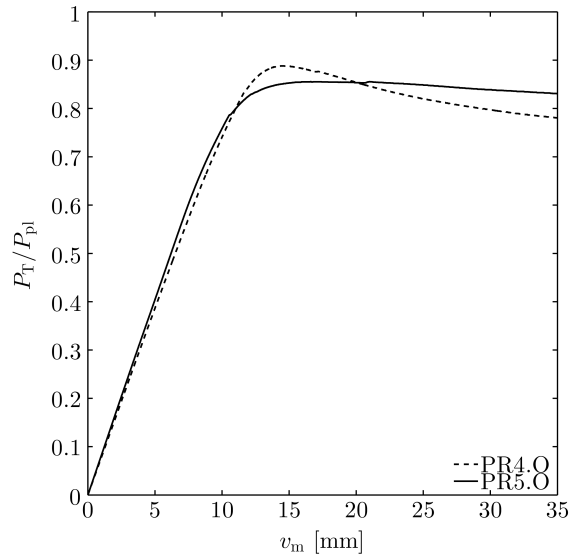
Figure 28: Normalised total load-maximum displacement curves for the outer loaded propped cantilevers

Despite the moments at the fixed supports exceeding the plastic moments, the total loads were still less than P_{pl}, as the span moments were significantly less than M_{pl}. For the outer loaded propped cantilevers, PR5.O and PR4.O shown in Fig. 28, PR4.O reached a higher normalised peak load of $P_u/P_{pl}=0.888$ compared to PR5.O which reached $P_u/P_{pl}=0.856$, and PR5.O reached its peak load at higher deflections and with a more gradual post-peak unloading region.

7 Conclusions

An experimental investigation of grade S355 structural steel rectangular hollow sections was performed, including tests on stub columns, simply supported beams, continuous beams and propped cantilevers. Two wall thicknesses of 5 mm and 4 mm were tested, giving class 1 and class 2 cross-sections respectively according to EN 1993-1-1 (2005) and compact cross-sections according to AISC 360-10 (2010). Tensile coupon tests revealed material yield stresses that were 10-20 % higher than the nominal values, with the 4 mm thickness coupons exhibiting both the highest yield and ultimate stresses, and the lowest ductility. Both coupon thicknesses displayed a yield plateau that extended up to a strain of approximately 3.5 %, after which strain hardening was observed. The stub column test specimens failed by local buckling at peak loads close to the yield load and at strains close to the yield strain, with the thicker specimens displaying a more gradual post-peak unloading. The stub columns did not exhibit ultimate axial loads influenced by strain hardening as average axial strains remained within the material yield plateau region. Similarly, tests on simply supported beams failed by local buckling and did not reach moments greater than the plastic moments.

The tests on statically indeterminate elements showed that system peak loads may occur at instances when cross-sections are undergoing unloading, having already reached their peak moments. The tests also showed that the system peak load need not occur when all critical

17

cross-sections have reached their peak moments, as the system can still have stiffness from cross-sections that are still loading. The propped cantilevers were fitted with post-yield strain gauges to measure the inelastic strains at the critical cross-sections associated with plastic hinges. The moment-rotation and moment-curvature curves showed increased moment capacities beyond the plastic moments at the fixed connection, due to the additional restraint provided to the cross-sections against local buckling. Plotting yield normalised hinge rotation-curvature curves, showed that rotations from an idealised plastic collapse geometry were proportional to curvatures only during the elastic loading phase, and that this relationship became rapidly non-linear once yielding had occurred.

The cross-section slenderness of the tested beams and the extended yield plateau of the structural steel, did not permit benefits from the strain hardening potential of the material, and so in such instances (ie. hot-rolled box sections) strain hardening should not generally be considered. Further investigations are required to understand the role of strain hardening on the structural response of steel sections of different cross-section shapes and formed through different process routes.

Acknowledgements

References

AISC 360-10 (2010). Specification for structural steel buildings. *American Institute of Steel Construction*, Chicago, IL 60601-1802. ANSI/ASIC 360-10

Alpsten G. A. (1968). Thermal residual stresses in hot-rolled steel members. *Fritz Laboratory Reports*, Paper 329.

Byfield M. P., Nethercot D. A. (1997). Material and geometric properties of structural steel for use in design. *The Structural Engineer*, 75(21):363–367.

Gardner L., Saari N., Wang F. (2010). Comparative experimental study of hot-rolled and cold-formed rectangular hollow sections. *Thin-Walled Structures*, 48:495–507.

EN 1993-1-1 (2005). Eurocode 3: Design of steel structures - Part 1-1: General rules and rules for buildings. *European Standard*, CEN:1–96.

Kemp A. R., Byfield M. P., Nethercot D. A. (2002). Effect of strain hardening on flexural properties of steel beams. *The Structural Engineer*, 80(8):188–197.

Byfield M. P., Nethercot D. A. (1998). An analysis of the true bending strength of steel beams. *Proceedings of the Institution of Civil Engineers - Structures and Buildings*, 128:188–197.

Gardner L., Wang F., Liew A. (2011). Influence of strain hardening on the behavior and design of steel structures. *International Journal of Structural Stability and Dynamics*, 11(5):855–875.

Centre for Advanced Structural Engineering (1990). Compressive tests of stainless steel tubular columns. Investigations Report s770, University of Sydney.

Wheeler A. T., Clarke M. J., Hancock G. J., Murray T.M. (1998). Design model for bolted moment end plate connections using rectangular hollow sections. *Journal of Structural Engineering ASCE*, 124(2):164–173.